

Structural Peculiarities of the AGN Object 1803+784

L. I. Matveyenko^{1*}, S. S. Sivakon¹, S. G. Jorstad^{2,3}, and A. P. Marscher²

¹*Space Research Institute, Russian Academy of Sciences, Profsoyuznaya ul. 84/32, Moscow, 117997 Russia*

²*Institute for Astrophysical Research, Boston University, 725 Commonwealth Avenue,
Boston, MA 02215-1401, USA*

³*Sobolev Astronomical Institute, St. Petersburg State University,
pr. Universitetskii 28, St. Petersburg, 198504 Russia*

Received September 22, 2009

Abstract—The structure of the AGN object 1803+784 has been investigated at a wavelength of 7 mm with a limiting angular resolution reaching $20 \mu\text{as}$. The ejector nozzle surrounded by a ring structure, an accretion disk, has been identified. The nozzle size is ~ 0.1 pc, the diameter of the ring structure is ~ 1.4 pc, and its width is ~ 0.25 pc. The reaction of the plasma flow produces a multimode precession responsible for the conical helical structure of the jet with a variable step and a curved axis. The viewing angle of the flow ejection is $\sim 40^\circ$. The central part of the ejected flow moving along the axis accelerates to a relativistic velocity. The apparent velocity reaches 12 s at a distance of ~ 1 mas or ~ 6 pc from the ejector. The outer part of the flow moves along a helix around a high-velocity component whose step is a factor of 4 smaller, because the longitudinal velocity is relatively low. The plasma is ejected almost toward the observer, as confirmed by its high brightness temperature $T_b \approx 8 \times 10^{13}$ K and highly beamed emission. The polarized emission from the nozzle is axisymmetric. The orientation of the polarization of the flow along the whole length is aligned with the direction of its motion, suggesting the excitation of a ring magnetic field around it and self-focusing.

DOI: 10.1134/S1063773710030011

Key words: AGN, accretion disk, ejector, precession, helical jet, self-focusing, aligned polarization.

INTRODUCTION

The characteristic structure of active galactic nuclei (AGNs) consists of a bright compact source—a core and a jet—a relativistic plasma flow. In some cases, the flow is twisted like a rope (M 87); in other cases, it forms a diverging conical helix with an increasing step and a curved axis (the quasar 3C 345 and the object 1803+784). The observed structural peculiarities of the jet are determined by the multimode precession of the ejector axis produced by the flow reaction (Matveyenko and Witzel 1999). Theoretical and laboratory studies have confirmed the formation of a helical jet structure under the action of a perturbing force (Hardee 2005). The helical structure of the jet in the source 1803+784 was investigated in detail by Britzen et al. (2001), Jorstad et al. (2005), and Matveyenko et al. (2008). This is a BL Lac object with weak emission lines (Lawrence et al. 1987; Homan and Lister 2006); its redshift is $z = 0.68$ and 1 mas corresponds to ~ 6.08 pc for the cosmological parameters $H_0 = 65 \text{ km s}^{-1} \text{ Mpc}^{-1}$

and $q_0 = 0.5$ (Britzen et al. 2005). The studies of its fine structure at centimeter and decimeter wavelengths have revealed individual jet fragments. Their visibility is determined by the optical depth of the relativistic plasma flow and by the transparency of the surrounding H II region, which vary with frequency and distance from the core (Marscher 2008). At a wavelength of 18 cm, the jet in 1803+784 is observed at distances up to 15 mas or 90 pc. At the same time, its synchrotron radio emission in the ejector region is attenuated by more than 30 dB. At millimeter wavelengths, the absorption is relatively weak. The absorption in the surrounding thermal plasma is responsible for the low-frequency spectral cutoffs of the compact components adjacent to the core. The spectral indices of the low-frequency cutoffs lie within the range $\alpha = 3-4$, differing significantly from the limit determined by the reabsorption. The cutoff frequency lies within the millimeter wavelength range and is shifted toward the centimeter and decimeter wavelengths with increasing distance from the ejector (Matveyenko et al. 2008). Thus, at different wavelengths, we see different fragments of the jet in 1803+784 and a change in the core

*E-mail: matveen@iki.rssi.ru

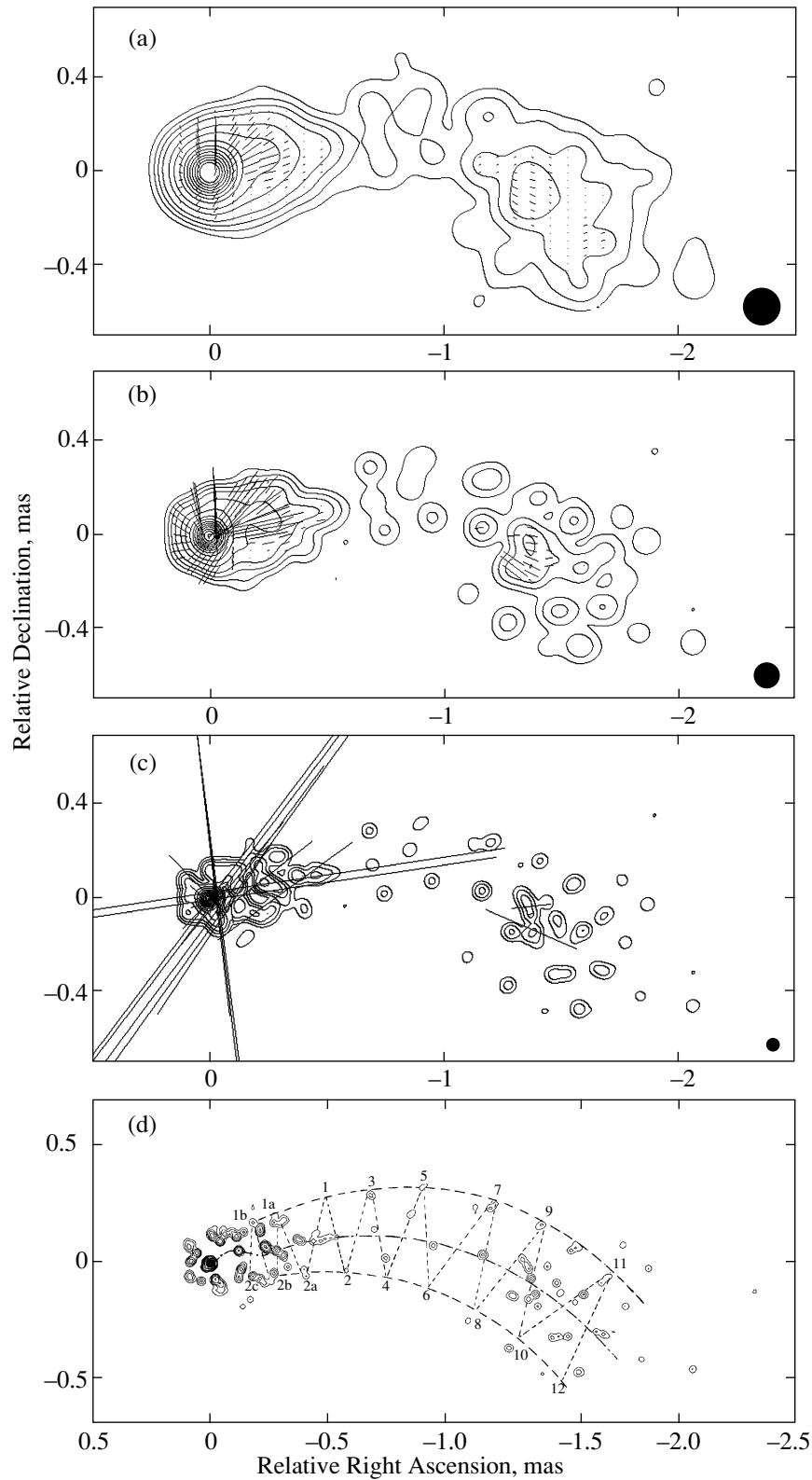


Fig. 1. Maps of the brightness distribution for the source 1803+784 at $\lambda = 7$ mm, the epoch is May 31, 1998. The isophotal levels are: 0.2, 0.5, 1.0, 2.0, 5.0, 10, 20, ..., 90, 99%. The map resolutions are: (a) 0.15 mas, $I_{\text{peak}} = 907$ mJy/beam, the polarized emission $P = 0.302$ Jy/beam/mas; (b) 0.10 mas, $I_{\text{peak}} = 840$ mJy/beam; (c) 0.05 mas, $I_{\text{peak}} = 749$ mJy/beam; (d) 0.02 mas, $I_{\text{peak}} = 570$ mJy/beam, the numbers denote the tangential helix directions; (e) 0.02 mas, $I_{\text{peak}} = 570$ mJy/beam, $P = 3.8$ mJy/beam/mas. (f) An averaged image of the maps with a resolution of 0.02 mas for the epoch 1998–2001. (g) An averaged image of the maps with a resolution of 0.05 mas for the epoch 1998–2001.

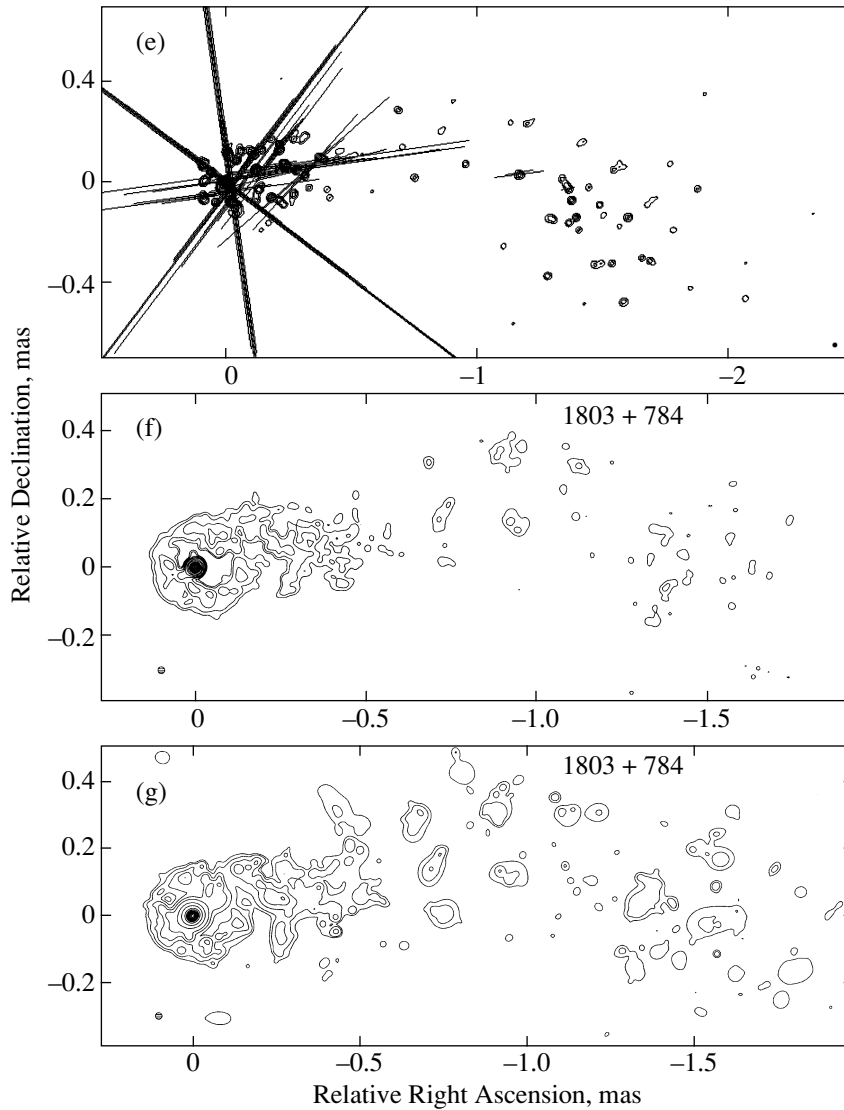


Fig. 1. (Contd.)

position. A variable step of the helical jet structure allowed them to be identified and combined into a single structure: a diverging conical helix with a variable step and an ejector located at the cone vertex. Its parameters and the relationship of the enhanced brightness of individual jet fragments to the periods of activity were determined. The helix step increases with distance from the core and decreases with time; the orientation of the axis also changes. The nozzle is the ejection region of the relativistic plasma flow; its formation into a highly collimated jet can be investigated only in the millimeter wavelength band. The regular long-term VLBA observations at 7 mm in the period 1998–2001 (17 epochs) extended significantly our knowledge of the processes in the core region. The jet structure was determined with an angular resolution of 0.15 mas, its individual components

were identified, and their superluminal velocities and kinematics were determined (Jorstad et al. 2005). Below, we investigate the superfine structure of the object 1803+784 based on these observational data.

THE JET

The observational data for the object 1803+784 at 7 mm (Jorstad et al. 2005) were processed with a step of $5 \mu\text{as}$. The brightness levels of the delta functions for the offset image were iterated with 10% discreteness. Next, the offset image was averaged with Gaussians of different widths. To identify low-brightness extended structures, the averaging was performed as before with a 0.15-mas-wide Gaussian beam. The intermediate and fine structures were investigated with higher resolutions reaching $20 \mu\text{as}$.

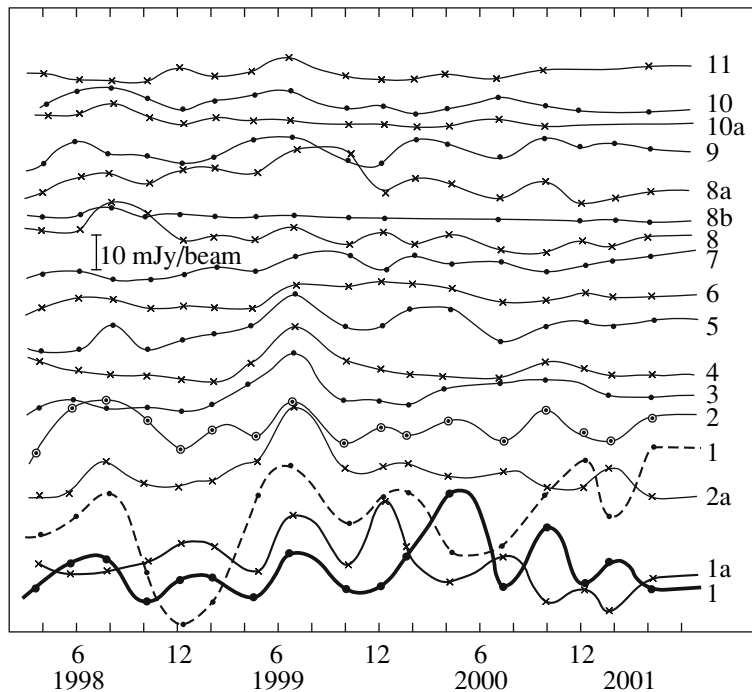


Fig. 2. Intensities of the helix components (Table 1). The dashed line corresponds to the emission from the ejector region (the factor is 0.1).

Consider the structure of the source with different angular resolutions for the epoch of May 31, 1998, as an example. A bright compact region—a core and a wide jet with a curved axis are identified on the map with the angular resolution $\varphi = 0.15$ mas (Fig. 1a). The jet is split approximately in two parts: the near part 0–0.6 mas in extent and the far part observed within 1.0–1.9 mas. The brightness of the intermediate region does not exceed 0.5% of its peak value equal to $I_{\text{peak}} = 907$ mJy/beam. This peculiarity is determined by the inhomogeneity of the relativistic plasma outflow. The axis of the near part of the jet is oriented in the plane of the sky at PA = -76° (the position angle is measured from the vertical line counterclockwise); the orientation of its far part corresponds to PA = -115° . Thus, the orientation changes by $\sim 40^\circ$. The jet width increases with distance from the core and reaches 0.5 mas.

The Helical Structure

As the angular resolution increases to 0.1 mas (Fig. 1b), the jet region immediately at the exit from the ejector and individual compact knots, including those located on both sides of the jet, are identified more clearly in the structure under consideration. The intensities of the components do not exceed $\leq 1\%$ of the peak value equal to $I_{\text{peak}} = 840$ mJy/beam and their sizes are ≤ 0.1 mas. As the resolution increases

to $\varphi = 0.05$ mas (Fig. 1c), their relative brightnesses are virtually kept at the previous level, $\leq 1\%$ of the peak value: $I_{\text{peak}} = 749$ mJy/beam. The VLBA high sensitivity and wide dynamic range made it possible to determine the intensities of the components under consideration with an accuracy of $\sim 10\%$.

The observed brightness temperature of the source rises with increasing angular resolution (decreasing φ), $T \sim T_b \varphi_s^2 / \varphi^2$, and reaches its limiting value at an angular resolution equal to the source's size: $\varphi = \varphi_s$. The relative emission from the components of the chains manifests itself most clearly on the maps with a resolution of 0.10–0.05 mas and corresponds to their angular sizes.

The mean sizes of the components increase approximately by a factor of 2 and reach 20 μas in the far part of the jet. Their relative positions are almost constant during the epochs 1998–2001 under consideration. The chains of components located on the jet sides correspond to the tangential directions of the turns of the diverging conical helix. They are marked by the numbers in Fig. 1d. The intensities of the components obtained from radio isophotes with an angular resolution of 0.1 mas are given in Table 1 and are graphically presented in Fig. 2: the dashed line corresponds to the emission from the ejector region reduced by a factor of 10. The intensities of the components are low, but they are kept constant within the error limits. The brightness distribution

Table 1. Brightnesses of the components of 1803+784 [mJy/beam], $\varphi = 0.1$ mas

| $t \setminus \setminus$ No. | I | 1a | 1 | 2a | 2 | 3 | 4 | 5 | 6 | 7 | 8 | 8a | 8b | 9 | 10 | 10a | 11 | 12 | 13 |
|-----------------------------|------|------|------|------|------|------|------|------|-----|------|-----|------|-----|-----|-----|-----|-----|-----|-----|
| Mar. 25, 1998 | 780 | 20.0 | 6.0 | 7.8 | 2.0 | 4.0 | 1.8 | 1.5 | 1.5 | 3.9 | 2.8 | 3.9 | 2.0 | 8.0 | 8.0 | 4.2 | 4.0 | 4.0 | 4.0 |
| May 31, 1998 | 840 | 17.0 | 8.0 | 8.0 | 1.7 | 4.2 | 4.2 | 1.7 | 4.2 | 4.5 | 8.0 | 8.4 | 1.7 | 8.5 | 8.3 | 4.2 | 1.7 | 4.0 | 1.0 |
| July 31, 1998 | 910 | 18.0 | 18.0 | 18.0 | 18.0 | 1.6 | 4.6 | 9.1 | 4.4 | 1.5 | 8.0 | 9.0 | 4.4 | 4.5 | 5.0 | 9.0 | 4.6 | 9.0 | 1.5 |
| Oct. 5, 1998 | 670 | 20.5 | 3.4 | 13.4 | 13.3 | 3.3 | 3.5 | 1.3 | 1.5 | 1.8 | 7.0 | 7.0 | 1.5 | 3.5 | 4.5 | 6.3 | 2.3 | 3.5 | 7.0 |
| Dec. 10, 1998 | 520 | 26.0 | 10.4 | 5.0 | 5.2 | 2.6 | 2.5 | 5.2 | 2.6 | 4.6 | 2.0 | 10.2 | 2.5 | 4.0 | 4.6 | 5.3 | 5.0 | 3.0 | 5.0 |
| Feb. 13, 1999 | 590 | 25.0 | 12.0 | 12.0 | 10.7 | 2.9 | 2.5 | 5.8 | 2.9 | 5.8 | 5.9 | 11.7 | 1.8 | 3.0 | 5.6 | 2.9 | 2.5 | 3.0 | — |
| Apr. 29, 1999 | 900 | 18.0 | 5.7 | 18.0 | 9.0 | 9.0 | 8.0 | 9.0 | 1.8 | 4.5 | 4.9 | 10.0 | 1.8 | 9.0 | 8.0 | 1.8 | 4.0 | 8.0 | 1.5 |
| July 17, 1999 | 930 | 18.0 | 10.0 | 15.0 | 10.0 | 9.5 | 10.0 | 10.0 | 4.6 | 4.6 | 2.5 | 8.0 | 0.8 | 2.0 | 2.0 | 1.5 | 2.0 | 2.0 | — |
| Oct. 6, 1999 | 830 | 20.0 | 8.3 | 16.6 | 8.3 | 4.1 | 8.2 | 8.8 | 8.8 | 9.0 | 4.1 | 16.0 | 1.7 | 4.0 | 4.0 | 1.0 | 3.0 | 3.0 | 2.0 |
| Dec. 5, 1999 | 900 | 40.0 | 9.1 | 18.0 | 12.0 | 4.5 | 4.5 | 8.5 | 9.0 | 4.5 | 4.5 | 4.5 | 1.5 | 4.5 | 8.0 | 4.5 | 2.5 | 4.0 | 2.0 |
| Jan. 24, 2000 | 913 | 40.0 | 18.0 | 18.0 | 9.2 | 4.6 | 4.6 | 14.0 | 9.1 | 9.0 | 5.0 | 5.0 | 1.5 | 9.2 | 8.0 | 1.8 | 4.8 | 2.0 | 2.0 |
| Apr. 5, 2000 | 740 | 14.8 | 3.7 | 14.5 | 10.0 | 3.7 | 3.7 | 10.0 | 7.5 | 7.5 | 8.0 | 8.0 | 1.5 | 7.5 | 7.5 | 4.5 | 3.7 | 3.5 | 3.5 |
| July 17, 2000 | 760 | 30.0 | 8.0 | 15.2 | 7.8 | 7.6 | 2.5 | 3.8 | 3.8 | 7.6 | 3.8 | 2.5 | 2.0 | 3.5 | 3.6 | 3.5 | 1.5 | 6.0 | — |
| Oct. 1, 2000 | 912 | 9.2 | 9.5 | 10.0 | 18.0 | 9.0 | 8.5 | 9.0 | 4.6 | 4.6 | 4.0 | 9.0 | 4.0 | 9.0 | 4.5 | 1.7 | 4.4 | 2.0 | 2.0 |
| Dec. 11, 2000 | 1020 | 20.3 | 10.3 | 10.0 | 10.5 | 10.2 | 6.1 | 10.5 | 6.0 | 6.1 | 4.0 | 2.0 | 1.0 | 6.1 | 5.0 | 5.0 | 5.0 | 2.0 | 4.0 |
| Jan. 28, 2001 | 845 | 15.5 | 4.0 | 17.0 | 8.5 | 6.8 | 4.2 | 8.5 | 5.0 | 8.4 | 4.5 | 4.0 | 1.0 | 4.5 | 2.0 | 2.0 | 2.0 | — | — |
| Apr. 14, 2001 | 1050 | 16.5 | 8.3 | 20.0 | 10.5 | 5.3 | 5.0 | 10.5 | 5.4 | 10.0 | 5.0 | 5.5 | 5.0 | 5.4 | 8.0 | 5.0 | 5.5 | — | — |
| I mean | — | 23.3 | 10.0 | 15.0 | 10.2 | 6.2 | 5.5 | 7.5 | 5.1 | 6.0 | 4.8 | 7.8 | 2.1 | 5.8 | 5.8 | 4.1 | 3.6 | 4.0 | 2.9 |
| $T_b, 10^9$ K | — | 21 | 9 | 13.4 | 9.2 | 5.5 | 5.0 | 6.8 | 4.6 | 5.4 | 4.3 | 7.0 | 1.9 | 5.2 | 5.2 | 3.7 | 3.2 | 3.6 | 2.6 |

Table 2. Brightnesses of the components [mJy/beam], $\varphi = 0.05$ mas

| $t \setminus \setminus$ No. | I | 1a | 1 | 2a | 2 | 3 | 4 | 5 | 6 | 7 | 8 | 8a | 8b | 9 | 10 | 10a | 11 |
|-----------------------------|-----|------|------|------|------|------|------|------|-----|------|------|------|-----|------|------|-----|------|
| ρ , mas | 0.0 | 0.32 | 0.49 | 0.4 | 0.58 | 0.69 | 0.76 | 0.9 | 1.0 | 1.15 | 1.27 | 1.16 | 1.3 | 1.35 | 1.48 | 1.7 | 1.57 |
| Mar. 25, 1998 | 702 | 18.0 | 6.5 | 7.0 | 1.8 | 1.4 | 7.0 | 1.4 | 1.4 | 3.5 | 7.0 | 3.5 | 1.4 | 1.4 | 3.6 | 3.8 | 3.6 |
| May 31, 1998 | 756 | 15.3 | 15.3 | 9.0 | 1.7 | 3.6 | 3.6 | 1.5 | 3.8 | 4.1 | 7.5 | 7.6 | 1.5 | 7.6 | 7.5 | 3.8 | 1.5 |
| July 31, 1998 | 820 | 18.0 | 16.2 | 16.2 | 16.2 | 1.4 | 4.1 | 8.1 | 4.0 | 1.4 | 15.3 | 8.0 | 4.0 | 4.1 | 8.0 | 8.0 | 1.4 |
| Oct. 5, 1998 | 603 | 18.1 | 3.1 | 12.1 | 12.0 | 3.0 | 3.2 | 1.1 | 1.1 | 1.6 | 12.1 | 6.0 | 1.4 | 3.4 | 5.8 | 3.0 | 1.2 |
| Dec. 10, 1998 | 468 | 23.0 | 9.3 | 9.4 | 4.6 | 2.3 | 2.2 | 4.7 | 2.3 | 2.3 | 4.7 | 9.1 | 2.3 | 0.9 | 2.3 | 2.2 | 5.0 |
| Feb. 13, 1999 | 531 | 26.1 | 10.8 | 10.8 | 9.6 | 2.6 | 2.3 | 5.2 | 2.6 | 5.2 | 5.3 | 10.7 | 1.1 | 2.7 | 5.0 | 2.6 | 2.3 |
| Apr. 29, 1999 | 810 | 16.2 | 5.1 | 16.2 | 8.1 | 8.1 | 7.2 | 8.1 | 1.6 | 4.1 | 4.4 | 9.0 | 1.6 | 8.1 | 7.2 | 1.6 | 3.6 |
| July 17, 1999 | 838 | 23.0 | 17.1 | 30.0 | 17.1 | 16.6 | 15.3 | 17.1 | 8.4 | 8.4 | 8.1 | 14.4 | 2.5 | 7.3 | 7.3 | 2.7 | 7.3 |
| Oct. 6, 1999 | 747 | 18.0 | 7.4 | 15.0 | 7.5 | 3.7 | 7.4 | 7.9 | 7.9 | 8.1 | 3.7 | 14.4 | 1.5 | 3.6 | 3.6 | 0.9 | 2.7 |
| Dec. 5, 1999 | 810 | 36.0 | 8.2 | 14.6 | 11.0 | 4.0 | 4.0 | 7.7 | 8.1 | 4.1 | 7.7 | 4.0 | 1.3 | 1.3 | 4.0 | 1.3 | 1.3 |
| Jan. 24, 2000 | 822 | 22.5 | 16.2 | 16.2 | 8.3 | 4.1 | 4.1 | 12.6 | 8.2 | 8.1 | 4.5 | 8.1 | — | 8.2 | 1.6 | 1.6 | 1.6 |
| Apr. 5, 2000 | 666 | 13.3 | 33.3 | 13.0 | 13.3 | 2.8 | 2.8 | 13.3 | 6.8 | 6.8 | 7.2 | 7.2 | — | 6.7 | 3.2 | 1.3 | 3.3 |
| July 17, 2000 | 684 | 19.8 | 7.2 | 13.7 | 7.0 | 6.8 | 1.4 | 3.4 | 3.4 | 6.8 | 3.4 | 3.2 | — | 3.2 | 6.8 | 3.2 | 1.4 |
| Oct. 1, 2000 | 820 | 8.3 | 24.7 | 9.0 | 16.0 | 8.1 | 7.7 | 8.1 | 4.0 | 4.0 | 4.0 | 8.1 | 3.6 | 8.1 | 4.0 | 1.5 | 4.0 |
| Dec. 11, 2000 | 918 | 12.0 | 9.2 | 9.0 | 9.2 | 9.1 | 5.4 | 9.2 | 5.4 | 5.5 | 5.4 | 1.8 | — | 5.5 | 2.7 | — | — |
| Jan. 28, 2001 | 760 | 5.0 | 15.3 | 15.3 | 7.7 | 6.1 | 3.7 | 7.7 | 4.5 | 7.7 | 4.1 | 3.6 | — | 6.8 | — | — | — |
| Apr. 14, 2001 | 945 | 14.8 | 7.5 | 7.5 | 14.8 | 4.8 | 4.5 | 9.5 | 4.9 | 9.0 | 9.0 | 5.0 | — | 5.0 | 1.8 | — | 5.0 |
| $T, 10^9$ K | — | 16.4 | 12.5 | 13.2 | 9.7 | 5.2 | 5.1 | 7.4 | 4.6 | 5.3 | 6.7 | 7.3 | 1.6 | 4.9 | 4.4 | 2.2 | 2.7 |

Table 3. Parameters of the helix

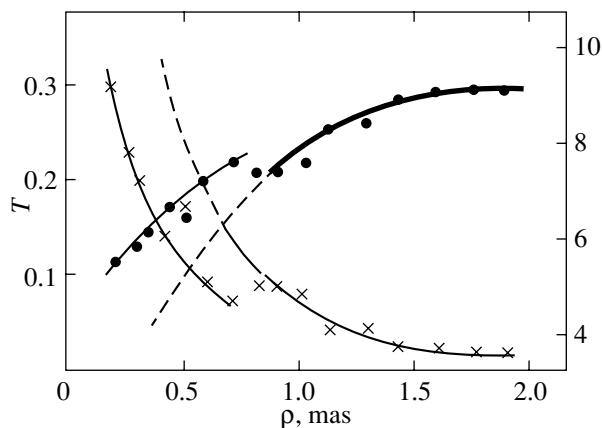
| No. | 1c | 2c | 1b | 2b | 1a | 2a | 1 | 2 | 3 |
|------------------------------|------|------|------|------|------|------|------|------|------|
| P , mas | 0.04 | 0.1 | 0.18 | 0.26 | 0.34 | 0.42 | 0.53 | 0.61 | 0.73 |
| H , mas | — | 0.14 | 0.15 | 0.16 | 0.16 | 0.19 | 0.19 | 0.20 | 0.23 |
| Ω , mas ⁻¹ | — | 7.1 | 6.7 | 6.3 | 6.3 | 5.3 | 5.3 | 5.0 | 4.3 |
| A , mas | 0.07 | 0.07 | 0.1 | 0.11 | 0.11 | 0.14 | 0.12 | 0.14 | 0.14 |
| Q , deg | 67 | 35 | 29 | 23 | 18 | 18 | 13 | 13 | 11 |
| Ξ , deg | -20 | -20 | -15 | -13 | -12 | -4 | -4 | 0 | 0 |

| No. | 4 | 5 | 6 | 7 | 8 | 9 | 10 | 11 | 12 | 13 |
|------------------------------|------|------|------|------|------|------|------|------|------|------|
| P , mas | 0.84 | 0.94 | 1.04 | 1.15 | 1.25 | 1.40 | 1.56 | 1.72 | 1.9 | 2.2 |
| H , mas | 0.21 | 0.20 | 0.21 | 0.21 | 0.25 | 0.31 | 0.32 | 0.34 | 0.30 | — |
| Ω , mas ⁻¹ | 4.8 | 5.0 | 4.8 | 4.8 | 4.0 | 3.2 | 3.1 | 2.9 | 3.3 | — |
| A , mas | 0.13 | 0.15 | 0.12 | 0.12 | 0.12 | 0.14 | 0.14 | 0.14 | 0.14 | 0.14 |
| Q , deg | 8.8 | 9 | 6.6 | 6.0 | 5.5 | 5.7 | 5.1 | 4.6 | 4.2 | 3.6 |
| Ξ , deg | 3 | 3 | 8 | 13 | 14 | 15 | 21 | 22 | 23 | 24 |

Note. $T(\rho)$ is the period, $\Omega(\rho) \sim 1/T$ is the angular velocity, $A(\rho)$ is the amplitude of the helix turn, $Q = \arctan A/\rho$ [deg] is the amplitude viewing angle, $\xi(\rho)$ is the orientation of the helix axis.

in the components and their sizes are determined by the optical depth—the number of relativistic electrons along the line of sight. The optical depth varies within the cross section of the helix turn and determines the fine structure and total size of the source corresponding to the cross section of the turn. As the angular resolution increases to $\varphi = 0.02$ mas, compact knots are observed in the source (see Fig. 1d).

The chains of components correspond to a diverging conical helix whose step $H(t)$ increases with distance from the core (Table 3, Fig. 1d). Given the curvature of the helix axis, the step was determined from

**Fig. 3.** Step T and angular velocity of precession Ω versus distance ρ .

the separations between the projections of the chains of components onto its axis. In the far part of the jet, $1 \text{ mas} \geq \rho \geq 2 \text{ mas}$, the step changes from 0.22 to 0.30 mas. In the region of reduced brightness ($\rho \approx 0.9 \text{ mas}$), the step changes only slightly and then decreases to 0.12 mas as the core is approached (Fig. 3). The helix step is determined by the precession period $T(t)$ and the longitudinal flow velocity $V(t)$ —the precession angle. For a constant velocity, the step $H(t)$ corresponds to $T(t)$ and the angular velocity of precession is $\Omega(t) \sim 1/T(t)$. We see from Fig. 3 that the helix step changes exponentially in the periods of enhanced activity. If we exclude the zone of silence $\rho \approx 0.8\text{--}1.0 \text{ mas}$, then the helix step changes with distance ρ exponentially, as indicated by the dashed line. At a constant flow velocity, the time t is proportional to the distance $(\rho_0 - \rho)$ measured from the jet head ρ_0 . In this case, $\Omega = 3.3 + 1.17t^{3.27}$, i.e., the angular velocity of precession is almost proportional to the time cubed. The cubic time dependence of the angular velocity results from the continuous action of the flow reactive force, including the increase in the precession angle of the perturbing force. The helix has a small conicity; its diameter increases from 0.25 mas near the core to 0.35 mas in the far part.

The reaction of the ejected flow produces a multimode precession of the ejector axis in the object 1803+784. The first mode causes a curvature of the jet axis that changes from PA = -180° in the far part, $\rho \approx 50''$, to PA = -75° near the ejector, $\rho \approx$

0.15 mas. The second mode is responsible for the diverging helical shape of the jet with an increasing step and is observed at distances up to 90 pc at decimeter wavelengths. The helix step increases linearly with distance. However, a deviation from the linear dependence is possible in the near part of the jet. The ratio of the mean angular velocities of these modes is ~ 30 (Matveyenko et al. 2008).

As follows from these results, the jet near the ejector, $0.3 \text{ mas} \leq \rho \leq 1.5 \text{ mas}$, is surrounded by an outer helical structure whose step is approximately a factor of 4 shorter than that of the inner helix. This difference can be determined both by the difference in flow velocities and by the modes of the angular velocities of precession. As will be shown below, the former case is more likely.

Brightness Temperatures of the Outer Helix Components

The chains of components, the tangential directions of the jet-framing helix turns, manifest themselves as the angular resolution increases. The brightnesses of the components on the maps with a resolution up to 0.1 and 0.05 mas reach several percent of the peak value. Their relative emission is virtually kept constant within the limits of the measurement errors. Tables 1 and 2 give the intensities of the ejector I and components 1–13 in mJy/beam, while the lower rows list their mean values and brightness temperatures T_b in 10^9 K during the series of observations. The brightness temperatures of the components virtually coincide in both cases, which is indicative of the resolution of the components, i.e., their sizes are 0.05–0.10 mas. The mean intensities of the components decrease from 23 mJy/beam near the core to $\sim 4 \text{ mJy/beam}$ in the far part, corresponding to brightness temperatures of $(20 - 3) \times 10^9 \text{ K}$ (Fig. 4). The brightness temperatures of the components decrease relative to the peak value to $T_b \approx 16 \times 10^9 \text{ K}$ at $\rho = 0.3 \text{ mas}$ and to $T_b \approx 3 \times 10^9 \text{ K}$ in the far part. The change in temperature is exponential and corresponds to $T_b(10^9, \text{ K}) = 3.5 + 24\rho^{-2.2} \text{ K}$. The brightness temperatures of two components at the epoch of reduced activity, $\rho \approx 0.75 \text{ mas}$, do not exceed $5 \times 10^9 \text{ K}$ and are close to those of the components in the far part of the helix, $\rho \approx 1.6 \text{ mas}$. It can be assumed that if the relativistic plasma were ejected continuously, then the change in component brightness with distance ρ would be in the form of a gradual decline corresponding to the dashed line in Fig. 4. For a constant flow velocity, the expected change in component brightness temperature with time $t = 1.4 - \rho$ corresponds to $T_b(10^9, \text{ K}) \approx 4 + 14t^2$.

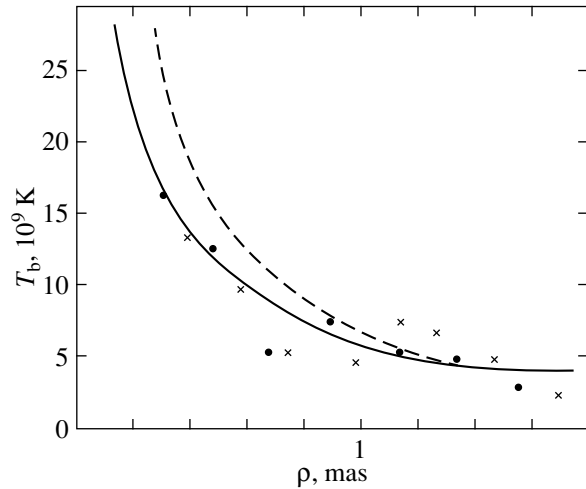


Fig. 4. Brightness temperatures of the components in the jet versus distance ρ , the epoch is May 31, 1998. The dashed line corresponds to the case of a continuous core activity.

The reduction in component brightness temperature is determined by the lifetime of the high-energy electrons and by the change in the diameter and cross section of the helix turns—the flow, the magnetic field. The size of the components—the thickness of the distant helix turns—increases by a factor of ~ 2 , while their diameter increases by a factor of ~ 1.5 .

The upper limit for the velocity of the flow moving along the outer helix can be estimated from the component brightness temperatures. The synchrotron emission from a flow moving with a relativistic velocity is highly beamed. In the case of a relativistic flow velocity, the brightnesses of the components—the tangential directions of the helix corresponding to the flow motion toward the observer—will be considerably higher than those when moving in the opposite direction. Accordingly, the brightnesses of the components in the upper (crosses) and lower (circles) parts of the helix must differ from each other. Actually, however, no differences between the brightness temperatures of both chains are observed (Fig. 4). No superluminal motions of the components in the outer helix are observed either. However, this does not apply to the high-velocity component of the flow moving along the helix axis and, hence, the helix step for the high-velocity flow is approximately a factor of 4 larger than the step of the outer helix. The central flow physically moves with a relativistic velocity v of the order of c (c is the speed of light). In this case, the longitudinal flow velocity for the outer helix v must be $\leq 0.25c$.

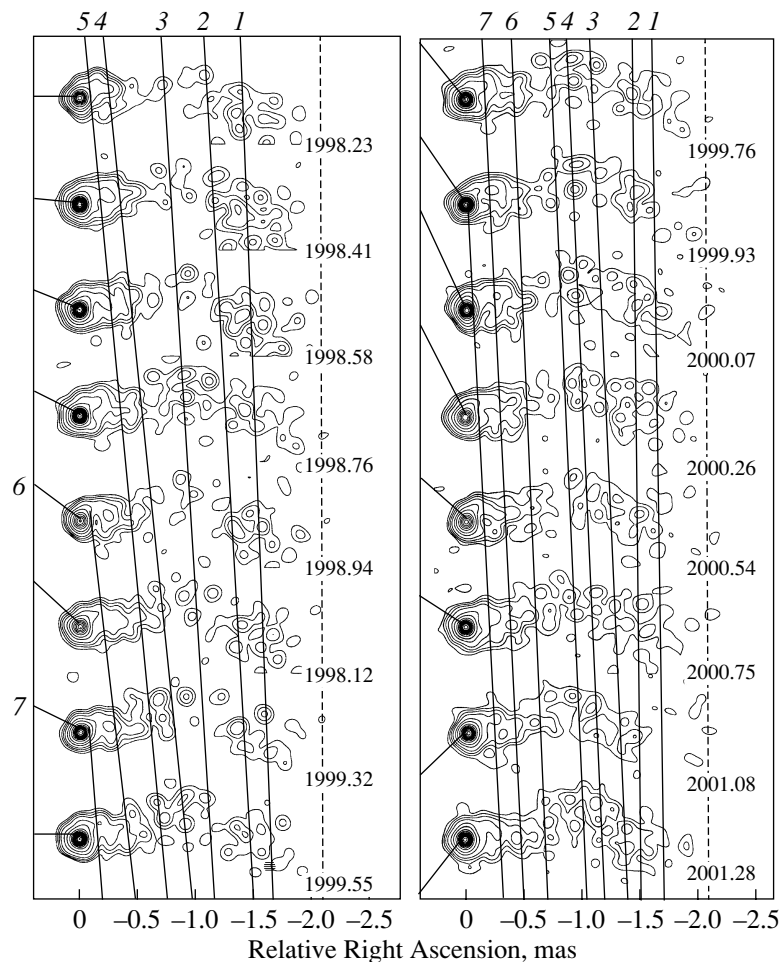


Fig. 5. Maps of the brightness distribution for the source 1803+784 at $\lambda = 7$ mm with a resolution of 0.10 mas at different epochs. The isophotal levels are: 0.2, 0.5, 1.0, 2.0, 5.0, 10, 20, ..., 90, 99%.

The Superluminal Central Component of the Jet Flow

Jorstad et al. (2005) determined the velocities of individual fragments in the jet of 1803+784 and the kinematics of their motion. The apparent velocities of the two components located near the ejector exceed considerably the speed of light and reach ~ 15 c. Therefore, investigating the fine structure of the jet is of particular interest. The brightness distribution for the object 1803+784 at 7 mm over the period of observations under consideration with an angular resolution of 0.1 mas is presented in Fig. 5. On the whole, the jet is a weakly collimated relativistic plasma flow whose emission is traceable at distances up to 2 mas (~ 12 pc). At distances larger than 1.8 mas or ~ 35 light-years (ly), the radio emission at 7 mm is reduced significantly and virtually disappears. This is related to the energy losses by the high-energy electrons—their lifetime. In the limiting case, the velocity of the ejected central plasma flow is equal to the speed of light, $v \leq c$, and the lifetime of the relativistic

electrons will be $t \geq 35$ yr. In the local frame, the frequency at which the energy losses by the relativistic electrons through the synchrotron emission become significant is $f \sim B^{-3}t^{-2}$ GHz, where t is given in years (Kellermann 1974). For a frequency of 43 GHz, the limiting magnetic field is $B \leq 0.03$ G (Jorstad et al. 2005). The velocity of the emission region determined by the redshift z and the proper motion of the jet in the opposite direction does not affect significantly this magnetic field estimate. At distances larger than 2 mas, the emission from the relativistic electrons is observed at centimeter and decimeter wavelengths. The jet extension is a highly collimated helical flow with a variable step (Matveyenko et al. 2008).

At the beginning of the period 1998–2001 under consideration, the jet consists of two approximately equal parts (Fig. 5). The width of the division reaches ~ 0.6 mas or ~ 3.6 pc. The plasma flow moves along the helical jet axis (indicated by the dash-dotted line in Fig. 1d). The break in the jet is observed in the region where the axis is bent. In

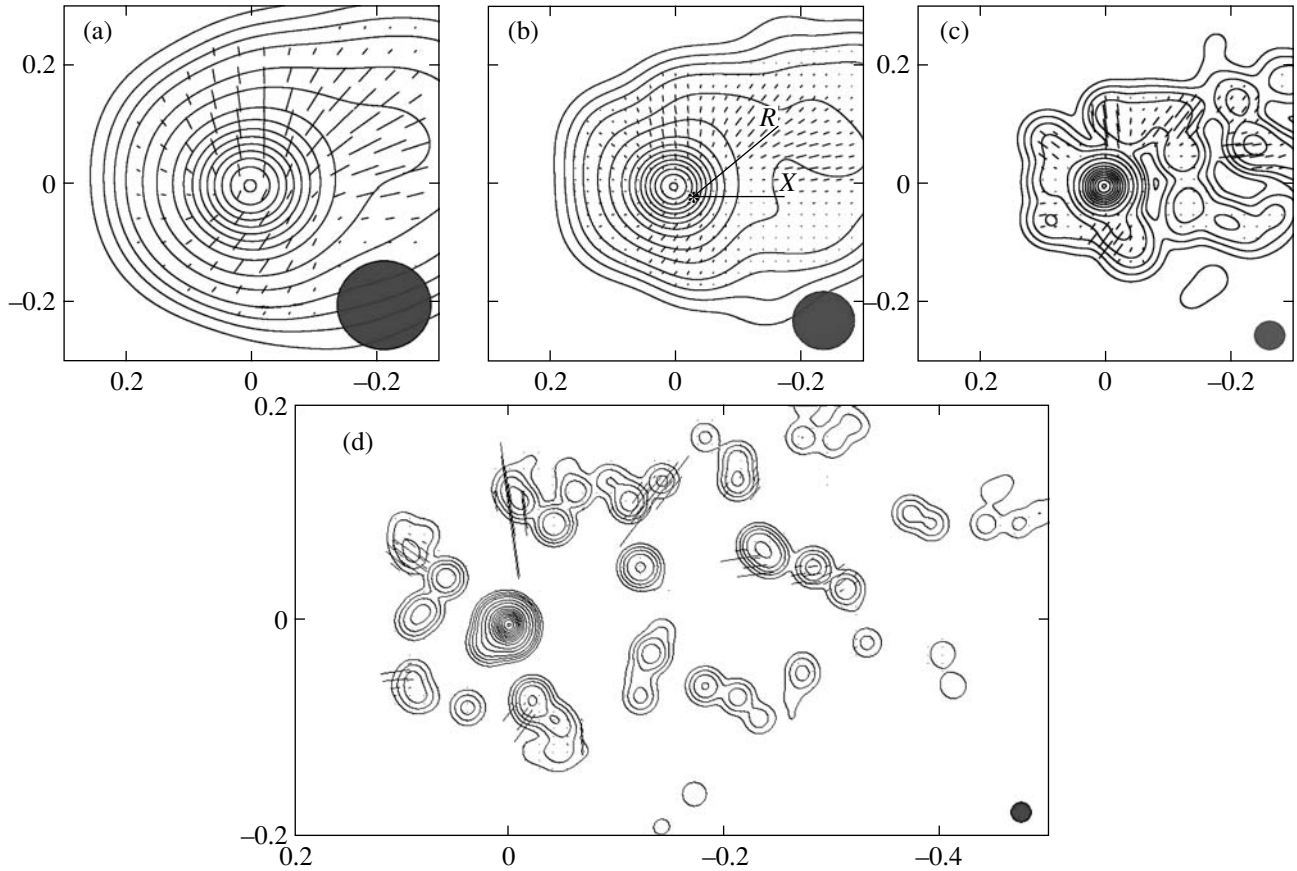


Fig. 6. Maps of the core region, the epoch is May 31, 1998. The isophotal levels are: 0.2, 0.5, 1.0, 2.0, 5.0, 10, 20, ..., 90, 99%. The map resolutions are: (a) 0.15 mas, $I_{\text{peak}} = 970$ mJy/beam, $P = 0.302$ Jy/beam/mas; (b) 0.10 mas, $I_{\text{peak}} = 839$ mJy/beam, $P = 0.280$ Jy/beam/mas; (c) 0.05 mas, $I_{\text{peak}} = 764$ mJy/beam, $P = 0.382$ Jy/beam/mas; (d) 0.02 mas, $I_{\text{peak}} = 570$ mJy/beam, $P = 28.5$ mJy/beam/mas.

the case of a highly beamed flow emission, this can lead to a significant attenuation of the apparent emission and can manifest itself as a jet break. However, after the epoch 1999.32, the division region begins to disappear and to fill with high-energy relativistic plasma electrons and the break disappears by the epoch 2000.75. Thus, the plasma flow fills the jet division region with a length of 3.6 pc or ~ 12 ly in a time ~ 1.4 yr, which corresponds to an apparent flow velocity $v \approx 8.5c$.

A high flow velocity must also be observed immediately at the exit from the ejector nozzle. Dense knots in the flow, bright sources, can be an indicator of this motion, which does not rule out the velocity difference between the knots and the flow. The main difficulty in determining the velocities of the knots is their identification at different epochs. A knot is a compact fragment of the flow with an enhanced density of relativistic electrons. The emission of the knots, along with the flow itself, changes with increasing distance from the ejector, their relative brightness changes, and a jet with a complex spatial structure is formed. The

highly beamed emission has an effect. This makes it difficult to distinguish and identify individual bright components. In Fig. 5, lines 1–7 connect the identified knots observed at different epochs. The image cores are connected with the corresponding instants on the time scale. Table 4 gives the times of observation of the fragments Δt in years, the distances traveled by them $\Delta \rho$ in light-years, and their apparent velocities v/c . Components nos. 1–4 located in the far part of the jet were ejected at preceding epochs of activity. Their velocities in the initial period (epochs 1998.23–1999.55) increase from $4.1c$ to $11.8c$ and, subsequently (epochs 1999.55–2001.28), decrease to 1.2 – $5.4c$, i.e., the components decelerate. As would be expected, the velocities of the components decrease with a certain delay relative to one another: from the older (in time) no. 1 to the younger no. 4 (Table 5). Thus, the velocities of the components correlate with their positions. The velocity of component no. 4 will decrease to $1.2c$ when it reaches the position of component no. 1 observed at present.

Components nos. 5–8 refer to the second stage of

Table 4. Velocities of the knots in the flow

| Parameter\ No. | 1 | 2 | 3 | 4 |
|--------------------|----------------|----------------|----------------|----------------|
| Epochs | 8.23–9.55–1.28 | 8.23–9.55–1.28 | 8.23–9.55–1.28 | 8.23–9.55–1.28 |
| Δt , yr | 1.32/1.73 | 1.32/1.73 | 1.32/1.73 | 1.32/1.73 |
| $\Delta \rho$, ly | 5.5/2.0 | 8.5/1.4 | 9.1/6.2 | 15.6/9.4 |
| v/c | 4.1/1.2 | 6.4/0.8 | 6.9/3.6 | 11.8/5.4 |
| Parameter\ No. | 5 | 6 | 7 | 8 |
| Epochs | 8.23–9.55–1.28 | 8.94–1.28 | 9.32–1.28 | 9.93–1.28 |
| Δt , yr | 1.32/1.73 | 2.32 | 1.96 | 1.35 |
| $\Delta \rho$, ly | 14.0/5.9 | 9.5 | 5.6 | 3.0 |
| v/c | 10.6/3.4 | 4.1 | 2.9 | 2.2 |

Table 5. Core, polarization $m(\rho)$ [%] / orientation PA [deg], ρ [mas], φ [mas]

| $\varphi \backslash \rho$ | –0.3 | –0.25 | –0.20 | –0.15 | –0.10 | –0.05 | 0.0 | 0.07 | 0.11 | 0.16 | 0.21 | 0.25 | 0.31 |
|---------------------------|---------|---------|---------|---------|---------|---------|---------|---------|---------|--------|---------|---------|--------|
| 0.50 | 2.8/–34 | 2.9/–35 | 3.1/–37 | 2.9/–37 | 2.7/–37 | 2.6/–37 | 2.3/–37 | 3.1/–39 | 3.1/–40 | 4/–43 | 5.4/–49 | 6.4/–53 | 6.8–54 |
| 0.15 | – | – | 21/–32 | 11/–32 | 4/–36 | 1.5/–37 | 0.7/–14 | 1.9/–22 | 7/–43 | 23/–60 | 24/–70 | 37/–74 | – |
| 0.10 | – | – | – | 25/–32 | 23/–35 | 2/–35 | 0.1/– | 5/–2 | 11/–13 | 30/–40 | 40/–46 | 35/–63 | 23/–65 |
| 0.05 | – | – | – | – | 50/–37 | 9/–37 | <0.5/– | 1/–22 | 20/–44 | 44/–37 | – | 38/–82 | 19/–77 |

activity; they entered the jet region after the period of “silence.” In this case, we see the relativistic plasma flow immediately at the exit from the ejector. The velocity of these fragments begins to decrease with time from $10.6c$ to $2.2c$. This may be related to a reduction in the core activity, a decrease in the ejection rate. However, as has been mentioned above, the intensity of the ejector emission increases regularly by 100 mJy/beam during the period under consideration (Fig. 2). In reality, the observed decrease in velocity can be explained by an acceleration of the ejected relativistic plasma flow in the jet formation region at a distance up to 1 mas. This suggests an increase in the velocity of component no. 8 ejected with a velocity of $2.2c$ to $12c$ at the exit from the active zone. Of course, the relativistic velocity of the component along the helical trajectory can make changes in the apparent picture, along with a possible change of absorption in the H II region. The density of thermal electrons in the surrounding medium that determines the emission in emission lines reaches $N_e \sim 10^8 \text{ cm}^{-3}$ and the recombination time is negligible, $t \sim 10^5/N_e$ yr. In fact, this means that the characteristic time of change in screen transparency will be determined by its sizes and the impact time of the ionizing agent—the core activity.

The acceleration of the plasma flow in the active

zone suggests compensation of the emission losses. In this case, the lifetime of the electrons emitting at 43 GHz should be calculated after their escape from the active zone. Thus, over their lifetime, they traverse a distance ~ 0.8 mas or ~ 15 ly and the magnetic field limit will be $B \leq 0.05$ G.

THE CORE: THE RING—NOZZLE

The nature of AGNs is not completely clear. There exist many models, but all of them need to be confirmed experimentally. The main difficulty is their small angular size. The angular resolution of $20 \mu\text{as}$ we achieved overcomes this difficulty, revealing the fine structure of the core.

The Ejector Region

As the angular resolution increases to 0.05 mas, a bright compact source and fragments of the surrounding structure begin to manifest themselves in the core region (Fig. 1c). A bright compact source—the nozzle of the relativistic plasma ejector and its surrounding ring structure are clearly identified at a resolution of 0.02 mas (Fig. 1d). This region is shown on an enlarged scale in Fig. 6d. The bright central source is displaced southeastward relative to

Table 6. Core polarization m [%]/PA [deg], $\varphi = 0.02$ [mas]

| $t \setminus$ No. | J_0 | J | $\Delta R/\text{PA}$ | 1c | 2c | 1b | 2b | 1a |
|-------------------|----------|---------|----------------------|---------|---------|----------|---------|---------|
| Mar. 25, 1998 | 0.06/−18 | 4.5/−23 | 0.04/120 | 4.5/−28 | — | 8/−48 | — | 7.5/115 |
| May 31, 1998 | 0.15/−45 | 2.8/135 | 0.03/130 | 22/−40 | 2/−82 | 11/−32 | — | — |
| July 31, 1998 | 0.14/−35 | 15/120 | 0.04/130 | 25/−25 | 5/−15 | 8/−82 | 2/115 | — |
| Oct. 5, 1998 | 0.5/−162 | 3/173 | 0.04/127 | 6/−16 | 15/54 | 14/−20 | 10/86 | — |
| Dec. 10, 1998 | 0.15/−3 | 17/160 | 0.03/180 | 23/−29 | — | 15/−52 | 15/78 | 4.5/100 |
| Feb. 13, 1999 | 0.04/−68 | 11/116 | 0.04/135 | 3/−41 | 14/127 | 7/−54 | — | — |
| Apr. 29, 1999 | 0.4/−69 | 40/126 | 0.07/125 | 3/−24 | 40/86 | 26/−51 | 7.5/51 | 8/116 |
| July 17, 1999 | 0.1/−42 | 9/−45 | 0.03/135 | 9/−28 | 3/−45 | 5/−37 | 6/55 | 8/−70 |
| Oct. 6, 1999 | 0.05/−57 | 35/−54 | 0.03/135 | 1.5/−27 | 1.5/−35 | — | — | — |
| Dec. 5, 1999 | 0.8/−76 | 6/−78 | 0.04/135 | 1.5/−30 | 3/−116 | 1.5/−65 | — | 4/−70 |
| Jan. 24, 2000 | 0.6/−87 | 8/112 | 0.03/23 | 11/−93 | — | 12/−33 | 13/77 | 15/117 |
| Apr. 5, 2000 | 0.2/−86 | 22/49 | 0.03/165 | 7/−16 | 20/−31 | 6/−51 | 15/124 | 12/119 |
| July 17, 2000 | 0.2/−58 | 47/−28 | 0.05/165 | 11/−43 | 7/−23 | 16/−33 | 11/−25 | 25/122 |
| Oct. 1, 2000 | 0.2/−55 | 8/15 | 0.05/164 | 2.5/−51 | 2/−15 | 19/−23 | 11/−87 | — |
| Dec. 11, 2000 | 0.06/−90 | 28/−48 | 0.04/180 | — | — | 20/−50 | 6/−78 | — |
| Jan. 28, 2001 | 0.3/−48 | 3/−47 | 0.035/135 | 6/−47 | 6/−20 | — | — | — |
| Apr. 14, 2001 | 0.4/−48 | 8/−34 | 0.04/15 | 4/−20 | 1.5/−3 | — | — | — |
| Mean | 0.24/−62 | 9.7/−52 | 0.04/128 | 4.9/−38 | 5.8/−53 | 10.2/−41 | 7.2/−80 | 9.5/88 |

Note. J_0 is the ejector, J is the component adjacent to the ejector (ΔR [mas]/PA [deg]).

the center of the circumference by $\Delta R_0 \approx 0.04$ mas (0.25 pc), PA = 128° (Table 6). This source with an asymmetric shape corresponds to the ejector region—the nozzle and to the fragment of the relativistic plasma flow at its exit. The sizes of the source do not exceed ~ 0.02 mas or ~ 0.1 pc. The fragment of the ejected flow is observed southeastward at a distance up to 0.05 mas from the nozzle center.

Consider the intensity–brightness temperature relation for the compact source at various angular resolutions (Table 7). As the angular resolution increases from 0.15 to 0.02 mas, the intensity is reduced but the brightness temperature of the source rises, indicative of small angular sizes of the ejector. The apparent size of the compact source at half maximum at a resolution of 0.02 mas is 0.023 mas. In the Gaussian case, the source’s size is ~ 0.011 mas and its brightness temperature reaches $T_b \leq 80 \times 10^{12}$ K. The structure of the core—a compact nozzle and the projection of the jet fragment suggest the ejection of the relativistic plasma flow almost toward the observer with a small inclination in the southeastward direction. Further out, the flow turns northwestward and transforms into a jet (see Figs. 1c and 1d). The

viewing angle of the jet base (the projection onto the plane of the sky) relative to the nozzle is 40°–45°.

The components distributed along the ring around the nozzle essentially retain their brightnesses and relative positions (Fig. 6d). The brightness temperatures of the components do not exceed 1–2% of the peak value, $T_b \approx 10^{13}$ K (the epoch is May 1998). The images of the maps with a resolution of 0.05 and 0.02 mas averaged over the period under consideration are shown in Figs. 1f and 1g, respectively. The diameter of the ring structure, the disk, is $\varnothing \approx 0.23$ mas or ~ 1.4 pc and the ring width is ~ 0.04 mas or 0.25 pc.

THE POLARIZED EMISSION

The Core

The polarized emission from the object 1803+784 at a wavelength of 7 mm is determined by the core region and the far part of the jet (Jorstad et al. 2005). As we see on the map with an angular resolution of 0.15 mas (Fig. 1a) at the epoch of May 31, 1998, these

Table 7. Peak brightnesses [Jy/beam]/brightness temperatures [10^{12} K]

| $t \setminus \varphi$ | 0.02 | 0.05 | 0.10 | 0.15 |
|-----------------------|-----------|----------|-----------|----------|
| Mar. 25, 1998 | 0.59/13.2 | 0.71/2.5 | 0.78/0.7 | 0.84/0.3 |
| May 31, 1998 | 0.57/12.7 | 0.76/2.7 | 0.84/0.8 | 0.91/0.4 |
| July 31, 1998 | 0.71/15.7 | 0.83/3.0 | 0.91/0.8 | 0.99/0.4 |
| Oct. 5, 1998 | 0.55/12.1 | 0.61/2.2 | 0.67/0.6 | 0.72/0.3 |
| Dec. 10, 1998 | 0.43/9.6 | 0.48/1.7 | 0.52/0.5 | 0.55/0.2 |
| Feb. 13, 1999 | 0.54/12.0 | 0.56/2.0 | 0.58/0.5 | 0.63/0.2 |
| Apr. 29, 1999 | 0.61/13.5 | 0.79/2.8 | 0.89/0.8 | 0.97/0.4 |
| July 17, 1999 | 0.61/13.5 | 0.84/2.9 | 0.92/0.83 | 1.00/0.4 |
| Oct. 6, 1999 | 0.70/15.6 | 0.78/2.8 | 0.83/0.8 | 0.88/0.4 |
| Dec. 5, 1999 | 0.72/16.0 | 0.85/3.1 | 0.9/0.8 | 0.93/0.4 |
| Jan. 24, 2000 | 0.76/16.9 | 0.86/3.1 | 0.91/0.8 | 0.98/0.4 |
| Apr. 5, 2000 | 0.46/10.2 | 0.66/2.2 | 0.74/0.7 | 0.82/0.3 |
| July 17, 2000 | 0.68/15.1 | 0.70/2.4 | 0.76/0.7 | 0.82/0.3 |
| Oct. 1, 2000 | 0.65/14.4 | 0.84/2.9 | 0.92/0.8 | 0.98/0.4 |
| Dec. 11, 2000 | 0.88/19.6 | 0.98/3.4 | 1.02/0.9 | 1.05/0.4 |
| Jan. 28, 2001 | 0.65/14.4 | 0.78/2.8 | 0.85/0.8 | 0.91/0.4 |
| Apr. 14, 2001 | 0.75/16.8 | 0.96/3.4 | 1.05/0.9 | 1.13/0.5 |

are fairly extended structures, ~ 0.5 mas. The maximum of the polarized emission reaches $P \approx 20$ mJy in the core region and does not exceed $P \leq 4$ mJy in the jet. The polarization is aligned with the jet axis and corresponds to the orientation at the beginning, $PA = -46^\circ$, and in the far part, $PA = 70^\circ$. Note that the polarized emission is reduced as the core center is approached. Let us analyze the polarization distribution in this region (see Fig. 6a, the dash length corresponds to a polarized emission of $P = 0.302$ Jy/mas). The polarization levels m (in %) and the position angles (PA) for various angular resolutions φ are given in Table 5. Consider the changes in polarization in the southward direction (negative ρ) and along the jet (positive ρ). The polarization level at the core center on the map with an angular resolution of 0.15 mas does not exceed $m = 0.7\%$ and the orientation corresponds to $PA \approx -14^\circ$. In the southward direction, the polarization level increases and reaches $m = 21\%$ at $\rho = -0.2$ mas, while the position angle remains almost constant and is $PA = -35^\circ$. Similar changes also occur in the northward direction: the polarization level increases to $m = 37\%$ and the position angle is retained, $PA \approx 7^\circ$ (Fig. 6a). The polarization level also increases along the jet. At $\rho = 0.25$ mas, the polarization increases to $m = 37\%$, but, in contrast

to the previous cases, the polarization plane turns and reaches $PA = -74^\circ$ in the far part.

The polarization at the core center depends significantly on the angular resolution (Table 5, Figs. 6a–6c). The polarization level reaches 2.3% at a resolution of 0.5 mas and decreases to its lowest value of $\sim 0.1\%$ at a resolution of 0.10–0.05 mas. The position angle also changes from -37° to -14° . The higher the resolution, the faster the increase in the polarization level in the southward direction, but the position angle is retained as before. The changes along the jet are similar in pattern: the limiting polarization level and orientation are reached faster with increasing angular resolution. The polarization level in the far part of the jet, $\rho \geq 0.2$ mas, does not depend on the angular resolution, because the region has a fairly extended structure. The decrease in polarization at the core center with increasing angular resolution is indicative of small angular sizes of the central region and a low polarization of its emission.

Consider the changes in polarization during the entire 1998–2001 period of observations at an angular resolution of 0.1 mas. The polarized emission from the central part ($\rho = 0.0$ mas) does not exceed $m \leq 4\%$ and the orientation lies within the range $PA =$

Table 8. Core, polarization m [%/PA, [deg], $\varphi = 0.10$ [mas]]

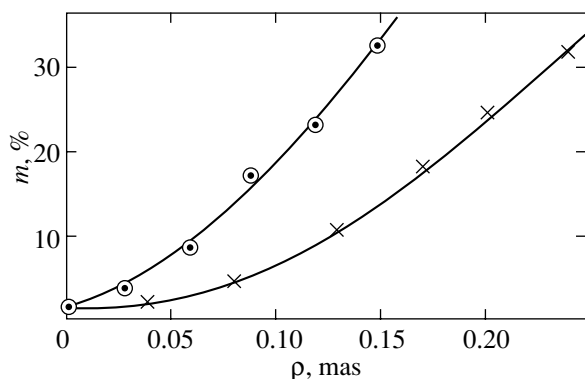
| $t \setminus \setminus \rho$ | -0.15 | 0.12 | -0.09 | -0.06 | -0.03 | 0.0 | 0.04 | 0.08 | 0.13 | 0.17 | 0.20 | 0.23 | 0.26 | 0.29 |
|------------------------------|--------|---------|--------|---------|---------|---------|---------|---------|--------|--------|--------|--------|--------|--------|
| Mar. 25, 1998 | 19/-13 | 20/-15 | 23/-21 | 12/-23 | 5/-31 | 2.4/-35 | 2/-37 | 9/-38 | 24/-43 | 23/-43 | 24/-48 | 43/-50 | 56/-53 | 16/-58 |
| May 31, 1998 | 25/-32 | 23/-35 | 14/-38 | 3/-35 | 1/-37 | 0.1/- | 0.9/-8 | 5/-2 | 15/-21 | 32/-40 | 40/-47 | 35/-57 | 35/-65 | 23/-65 |
| July 31, 1998 | 29/-14 | 29/-24 | 34/-35 | 12/-40 | 7/-46 | 3.7/-51 | 2/-48 | 4/-21 | 20/-14 | 30/-14 | 16/-28 | 20/-32 | 46/-58 | 14/-60 |
| Oct. 5, 1998 | - | 80/-22 | 20/-25 | 5.4/-25 | 1.6/-24 | 0.4/-22 | 0.3/-15 | 4/-25 | 11/-27 | 17/-28 | 26/-40 | 17/-55 | 26/-68 | 25/-70 |
| Dec. 10, 1998 | 58/-30 | 23/-30 | 23/-30 | 8/-30 | 4/-30 | 1.7/-25 | 2/-3 | 8/3 | 20/-5 | 30/-13 | 34/-27 | 25/-65 | 25/-85 | 46/-95 |
| Feb. 13, 1999 | 43/-20 | 34/-30 | 26/-39 | 8/-45 | 4.5/-59 | 3.5/-56 | 1.1/-58 | 1/-37 | 9/61 | 14/-52 | 26/-61 | 34/-61 | 26/86 | 30/85 |
| Apr. 29, 1999 | - | 6/-44 | 11/-52 | 6/36 | 5/-56 | 3.4/-59 | 2/-61 | 2/-44 | 15/-14 | 15/-24 | 15/-49 | 20/36 | 10/-70 | 7/-82 |
| July 17, 1999 | 72/-10 | 26/-19 | 18/-32 | 11/-35 | 1.5/-47 | 2/-48 | 1.5/-43 | 1.5/-44 | 5/-37 | 11/-27 | 50/-35 | 43/-47 | 25/-80 | 25/0 |
| Oct. 6, 1999 | 29/0 | 8.7/-25 | 29/-42 | 12/-42 | 6/-48 | 3.2/-50 | 2/-64 | 10/-47 | 26/-44 | 29/-45 | 60/-48 | 58/-49 | 50/-55 | 29/-85 |
| Dec. 5, 1999 | - | 3.6/-35 | 4/-35 | 6/-44 | 4/-45 | 4/-50 | 6/-56 | 6/-58 | 1.5/0 | 9/0 | 17/0 | 20/-30 | 29/-43 | 29/-45 |
| Jan. 24, 2000 | 4/-48 | 38/-53 | 3/-58 | 3/-61 | 4/-73 | 4/-88 | 3/85 | 20/84 | 9/-14 | 23/-48 | 23/-48 | 23/-48 | 7/-53 | - |
| Apr. 5, 2000 | 34/-31 | 25/-36 | 12/-39 | 5/-44 | 3/-59 | 2/-76 | 3/-84 | 5/-41 | 11/-48 | 11/-46 | 29/-48 | 29/-51 | 21/-54 | - |
| July 17, 2000 | 43/-38 | 30/-43 | 14/-43 | 4/-43 | 2.5/-43 | 0.8/-48 | 0.2/-60 | 0.2/-42 | 3/-18 | 17/-36 | 14/-41 | 7/38 | 7/-25 | - |
| Oct. 1, 2000 | 40/-12 | 40/-10 | 17/-18 | 3/-40 | 2/-50 | 0.1/-57 | 0.7/-57 | 0.7/-27 | 9/-15 | 30/-34 | 20/-55 | 20/-58 | 29/-52 | - |
| Dec. 11, 2000 | - | 11/-45 | 20/-45 | 6/-45 | 1.5/-50 | 0.7/-65 | 0.5/-50 | 0.2/-50 | 3/-50 | 4/-40 | 25/-45 | 50/-45 | 30/-50 | - |
| Jan. 28, 2001 | 20/-10 | 20/-16 | 18/-21 | 5/-39 | 3/-47 | 0.5/-45 | 3/-50 | 3/-50 | 6/-47 | 10/-40 | 10/-50 | 10/-52 | 10/-52 | - |
| Apr. 14, 2001 | 22/-15 | 12/-17 | 10/-22 | 6/-28 | 4/-32 | 0.4/-37 | 3/-35 | 2/-35 | 6/-42 | 20/-42 | 22/-45 | 15/-52 | 25/-67 | 25/-67 |
| Mean | 35/-18 | 23/-29 | 17/-35 | 8/-38 | 3.5/-46 | 1.9/-51 | 1.9/-48 | 4.6/-38 | 11/-29 | 18/-33 | 27/-37 | 28/-48 | 33/-60 | 24/-64 |

Table 9. Polarization orientation relative to the radius at the epoch of May 31, 1998, from the center of the circumference

| No. | 0 | 1 | 2 | 3 | 4 | 5 | 6 | 7 | 8 | 9 | 10 | 11 | 12 | 13 | 14 | 15 | 16 |
|--------------|---|----|----|----|-----|-----|-----|-----|-----|-----|-----|-----|-----|-----|-----|-----|-----|
| ξ , deg | 0 | 20 | 36 | 70 | 90 | 120 | 156 | 180 | 215 | 255 | 285 | 300 | 325 | 328 | 338 | 342 | 350 |
| Ψ , deg | 0 | 8 | -3 | -2 | -11 | -19 | -15 | -7 | -6 | -30 | -50 | -33 | -24 | -16 | -12 | -7 | 0 |

$-(22^\circ-76^\circ)$ (Table 8). The mean polarization levels are $m = 1.9\%$ and $PA = -51^\circ$. The mean polarizations in the southward direction reach $m = 35\%$, $PA = -18^\circ$ at $\rho = -0.15$ mas. Along the jet axis at $\rho = 0.26$ mas, the polarization increases to $m = 33\%$ and then decreases to $m = 24\%$. The polarization level increases exponentially, $m(\%) = 1.9 + 840\rho^{1.74}$ for the southward direction and $m(\%) = 1.9 + 440\rho^{1.94}$ along the jet (Fig. 7).

To a first approximation, as we see from Figs. 6a–6c, a radial polarization orientation is observed in the ring structure. The rough polarization center on the map with an angular resolution of 0.1 mas is denoted by the asterisk (Fig. 6b). This point is displaced by 0.04 mas southwest relative to the position of the brightness peak. Consider the change in polarization orientation Ψ relative to the radius R as a function of the azimuth ξ . We will take the distance from the center to be $\rho \approx 0.1$ mas. The orientation angle Ψ is measured from the radius counterclockwise. As we see from Fig. 8 (Table 9), the orientation angle relative to the radius remains equal to $-6^\circ \pm 4^\circ$ within the range of azimuths $\Delta\xi = 0^\circ-200^\circ$. At large azimuths, the emission has a polarization below its limiting value. Thus, the observed polarized emission from the core has an axisymmetric orientation. The observation of the compact source with an axisymmetric polarization orientation with a low angular resolution leads to a depolarization of the integrated emission in its central part.

**Fig. 7.** Distribution of polarization m in the core, the resolution is 0.10 mas: in the southward direction (circles) and along the jet (crosses).

The Nozzle—Accretion Disk

The observed peculiarities of the polarization of the core region suggest its complex structure that begins to manifest itself with increasing angular resolution. At a resolution of 0.05 mas, a compact source with an emission polarization below the detection limit is located in the central part (Fig. 5c). The polarized emission is determined by the fragments of the surrounding ring structure. The polarization of the fragments is oriented radially toward the central point southwest of the peak brightness. A further increase in angular resolution to 0.02 mas allowed us to determine the fine structure of the core and to identify its individual components (Fig. 1e). A bright compact source—the ejector nozzle and components of the ring structure—an accretion disk are identified at the center of the region. The polarization of the components lies within the range $m = 4-14\%$. The radial orientation of the component polarization is projected onto the center displaced by 0.04 mas southwest from the nozzle center (Fig. 6b).

The jet fragment J is observed immediately at the exit from the bright compact source—the ejector (Figs. 1d and 6d)). Table 6 gives the size and direction of the jet fragment R/PA , the degree and orientation of its polarization m/PA , and the levels of polarized emission from the nearby components 1_i-2_j . The level of polarized emission from the ejector J_0 at the epoch of May 31, 1998, is negligible, $m \leq 0.03\%$, and its mean value over the period under consideration does not exceed $m \leq 0.24\%$. At the same time, the level of polarized emission from the jet fragment J is $m \approx 10\%$; it reaches even $m \approx 30\%$ at the epochs of April 29, 1999, and January 28, 2001. Thus, the observed insignificant polarized emission from the ejector is actually determined by the “leakage” of the polarized emission from the jet fragment. The unpolarized emission from the flow at the exit from the ejector nozzle can actually be determined by an axisymmetric orientation of the polarization—a circular magnetic field enclosing the flow. An angular resolution exceeding the nozzle sizes, i.e., higher than several μas , is required to solve this question.

The size of the jet fragment at the exit from the nozzle does not exceed $R \leq 0.08$ mas, and its orientation, the direction of the ejector axis, lies within the range $120^\circ-160^\circ$. The orientation of the polarized

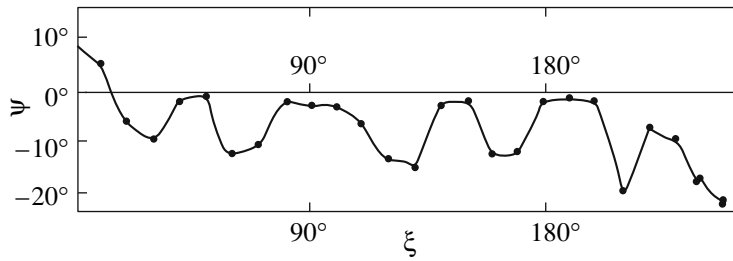


Fig. 8. Orientation of the polarization plane in the core relative to the radius, the resolution is 0.10 mas.

emission at the epoch of May 31, 1998, corresponds to $PA = 135^\circ$ and virtually coincides with the direction of the ejector axis $PA = 130^\circ$ and the direction of the relativistic plasma flow.

The mean polarization level of the components corresponding to the tangential directions of the initial turns of the outer helical structure, components 1n–2k (Table 6, Fig. 1d), lies within the range $m = 5\text{--}10\%$. The polarization of the emission from distant components is low and, in several cases, is below its limiting value. Their mean values do not exceed $m \leq 5\%$.

CONCLUSIONS

The galactic nuclei are surrounded by an ionized medium observed in optical emission lines. It absorbs the synchrotron radio emission that accompanies the active jet formation processes and limit the possibilities for investigating their nature. Since the transparency of the medium is fairly high at millimeter wavelengths, we can investigate the structure of the active region and determine the jet formation and ejection mechanism. The expected sizes of the active region can be of the order of one parsec. The angular resolution is a limiting factor in this case. Increasing the resolution to $20 \mu\text{as}$ or $\sim 0.1 \text{ pc}$ allowed the structure of this region to be studied in sufficient detail at a wavelength of 7 mm.

We established the following:

- the central bright source in the core is the ejector nozzle from which a relativistic plasma flow is ejected. The nozzle size is $\sim 10 \mu\text{as}$ or $\sim 0.06 \text{ pc}$;
- the ejector is surrounded by a ring structure whose radius is 1.4 pc and the ring width does not exceed 0.25 pc;
- the ring is determined by the emission of relativistic electrons and can be a constituent of the disk or the envelope;
- the disk is preferred, because it is an integral part of the structure related to the accretion of surrounding matter and its transformation into a jet flow;
- the relativistic plasma flow is ejected almost toward the observer with a small inclination in the

southeastward direction and then turns northwestward and transforms into a jet;

- the flow is ejected within an angle whose projection onto the plane of the sky is $40^\circ\text{--}45^\circ$;

- the central part of the ejected flow enters the active zone and accelerates to relativistic velocities. The apparent flow velocity is $\sim 12c$, while the apparent velocity of its individual knots can reach $15c$;

- the size of the acceleration zone reaches $\sim 5 \text{ pc}$ ($\sim 1 \text{ mas}$). The high-energy relativistic electrons after their escape from the active zone traverse a distance of $\sim 1.0 \text{ mas}$ or $\sim 15 \text{ ly}$, their lifetime does not exceed $t \leq 15 \text{ yr}$ and the generated magnetic field $B \leq 0.05 \text{ G}$;

- the reaction of the flow produces a multimode precession of the ejector axis responsible for the conical helical structure with a variable step and a curved axis;

- the outer part of the flow moves along the helix enclosing the jet;

- the step of the central helix is larger than that of the outer one by a factor of 4 due to the difference in their longitudinal and angular velocities;

- the emission from the relativistic plasma flow is linearly polarized, the polarization of the emission from the flow fragment at the exit from the nozzle reaches 30%;

- the orientation of the polarization of the high-velocity flow is aligned with the flow velocity over the whole length of the jet;

- the plasma flow excites a ring magnetic field (magnetic flux tube) and is self-focused;

- the flow is ejected from the nozzle toward the observer. The flow emission at the nozzle center is not polarized, $P < 0.04\%$, which is determined by an axisymmetric distribution of the polarization orientation and by the surrounding ring magnetic field;

- the high brightness temperature at the exit from the ejector nozzle, $T_b \approx 8 \times 10^{13} \text{ K}$, exceeds considerably the Compton limit and suggests that the emission is highly beamed and oriented almost toward the observer;

- the emission from the components of the disk ring structure is linearly polarized ($m \approx 4\text{--}11\%$) and

has a radial orientation, suggesting a ring magnetic field in the disk;

—the discovered structure of the core in the object 1803+784 (disk/jet) is similar to that of the core in the object NGC 4258 detected by maser emission lines (as in our case, the size of the accretion disk is ~ 1 pc, see Greenhill et al. 1993).

ACKNOWLEDGMENTS

This work was supported the “Origin and Evolution of Stars and Galaxies” Program of the Presidium of the Russian Academy of Sciences and the Russian Foundation for Basic Research (project no. 08-02-00154). L.I. Matveyenko thanks his colleagues for collaboration and hospitality.

REFERENCES

1. S. Britzen, T. P. Krichbaum, R. G. Strom, et al., *Astron. Astrophys.* **444**, 443 (2005).
2. S. Britzen, A. Witzel, T. Krichbaum, et al., *Pis'ma Astron. Zh.* **27**, 3 (2001) [*Astron. Lett.* **27**, 1 (2001)].
3. L. J. Greenhill, J. M. Moran, M. J. Reid, et al., *Astrophys. J.* **406**, 482 (1993).
4. P. E. Hardee, *AIP Conf. Proc.* **856**, 57 (2005).
5. D. C. Homan and M. L. Lister, *Astron. J.* **131**, 1262 (2006).
6. S. Jorstad, P. Marscher, L. Lister, et al., *Astron. J.* **130**, 1418 (2005).
7. K. Kellermann, *Galactic and Extra-Galactic Radio Astronomy* (Springer, Berlin, Heidelberg, 1974; Mir, Moscow, 1976), p. 527.
8. C. R. Lawrence, A. C. S. Readhead, T. J. Pearson, and S. C. Unwin, in *Superluminal Radio Sources*, Ed. by J. A. Zensus and T. J. Pearson (Cambridge Univ., Cambridge, 1987), p. 260.
9. A. Marscher, *ASPB Conf. Ser.* **386**, 437 (2008).
10. L. I. Matveyenko, S. Britzen, and D. A. Census, *Pis'ma Astron. Zh.* **34**, 83 (2008) [*Astron. Lett.* **34**, 69 (2008)].
11. L. I. Matveyenko and A. Witzel, *Pis'ma Astron. Zh.* **25**, 641 (1999).

Translated by V. Astakhov